Korean J. Chem. Eng., **27**(2), 375-384 (2010)
DOI: 10.1007/s11814-010-0112-z

REVIEW PAPER

Light management in dye-sensitized solar cell

Nam-Gyu Park†

School of Chemical Engineering, Sungkyunkwan University, Suwon 440-746, Korea
(*Received 11 December 2009 • accepted 16 December 2009*)

Abstract−Dye-sensitized solar cell (DSSC) is composed of a nanocrystalline TiO_2 film whose surface is covered with dye molecules, an iodide/tri-iodide electrolyte and a platinum counter electrode. Charge generation occurs when dye absorbs photon energy, which is separated by injection of photo-excited electrons into the conduction band of TiO_2. The photo-injected electrons are transported through TiO_2 network and collected at transparent conducting electrode. The oxidized dyes are regenerated by oxidation of iodide. Light-to-electricity conversion efficiency depends on photocurrent density, open-circuit voltage and fill factor. Photocurrent density is related to the incident photon-to-current conversion efficiency (IPCE) that is a collective measure of light harvesting, charge separation and charge collection efficiency. Since the higher IPCE, the higher photocurrent density becomes, light management in DSSC is one of most important issues. In this paper, effective methods to improve IPCE are described including size-dependent light scattering effect, bi-functionality design in material synthesis and panchromatic approach such as selective position of different dyes in a mesoporous TiO_2 film.

Key words: Dye-sensitized Solar Cell, Light Harvesting, Light Scattering, Bi-functional, Panchromatic

INTRODUCTION

Since the first discovery of the low-cost dye-sensitized solar cell (DSSC) in 1991 by Prof. Michael Gratzel and his coworker [1], it is regarded as one of the promising photovoltaic solar cells. Unlike solid p-n junction type solar cell, DSSC is categorized into photoelectrochemical type because it contains redox electrolyte. DSSC usually consists of a dye-adsorbed nanocrystalline TiO_2 film on a fluorine-doped tin oxide (FTO) substrate, an iodide/iodine redox electrolyte and a discontinuous platinum nanoparticles on a FTO substrate. To achieve high efficiency in DSSC, it is essential to prepare the mesoporous TiO_2 film with high surface area. In addition, packing density of TiO_2 film, dye purity and electrolyte composition are also important in terms of overall conversion efficiency. During past two decades, substantial progresses have been made. As a result, the solar-to-electricity conversion efficiency as high as 10-11% has been achieved [2-5]. Thanks to different colors from dye molecules and nano-sized inorganic oxide thin film, colorful and transparent appearance is possible for DSSC. Energy payback time of DSSC is analyzed to be about less than 0.8 year [6], while that of the multicrystalline silicon solar cell is about 3-4 years [7]. This indicates that DSSC is expected to be a promising solar cell for highly cost-effective solar power system.

1. DSSC Structure and Working Principle

Fig. 1 shows the structure and the working principle of DSSC. DSSC consists of the working electrode comprising a dye-adsorbed mesoporous TiO_2 film on a transparent conductive oxide (TCO) substrate, the platinum- and/or carbon-based counter electrode and the iodide/triiodide redox electrolyte. When light shines on DSSC, electrons on the ground state (or HOMO) of dye are excited to the excited state (or LUMO) of dye, which is refereed to charge generation step. The photo-excited electrons are injected in the conduction band of TiO_2 within pico- to femto-second, which is referred to as charge separation step. The photo-injected electrons are transported through the porous TiO_2 network with rate of about micro- to mili-second and eventually collected on TCO, which is referred to as charge collection step. Those three successive steps are essential for photocurrent generation. The oxidized dyes are regenerated by oxidation of iodide within nano-second time scale. Open-circuit voltage is generally determined by the energy difference between the Fermi level of TiO_2 and the redox electrolyte potential. Charge collection efficiency is not always 100% since photo-injected electron may recombine with the oxidized dye via surface state of TiO_2.

In DSSC, it is essential to match the energy level of each component. The conduction band of wide band gap material, such as TiO_2, lies on the position lower than the excited state of dye. In addition, the energy level of redox potential should be equal to or higher than the ground state of dye. Usually, the redox potential of the solution is hardly affected by the current and it is the same in both the dark and the light. Regarding electron transport, photo-injected electrons are transported by diffusion process because of lack of the built-in electric filed in the entire TiO_2 film. Under the circumstance of constant generation of photocharge and removal at the TCO contact, the Fermi energy level decreases in the direction of the TCO contact at short-circuit condition. However, at open-circuit condition the Fermi energy level is constant across the entire film [8]. Compared with the typical p-n junction solar cell, such as silicon solar cell, photoelectrochemical-type DSSC shows different photovoltaic action such that there is no significant space charge region, electric field is not important, and carries of only one type are presented in the oxide semiconductor [9].

2. Incident Photon-to-current Conversion Efficiency (IPCE)

Incident photon-to-current conversion efficiency (IPCE), which

†To whom correspondence should be addressed.
E-mail: npark@skku.edu

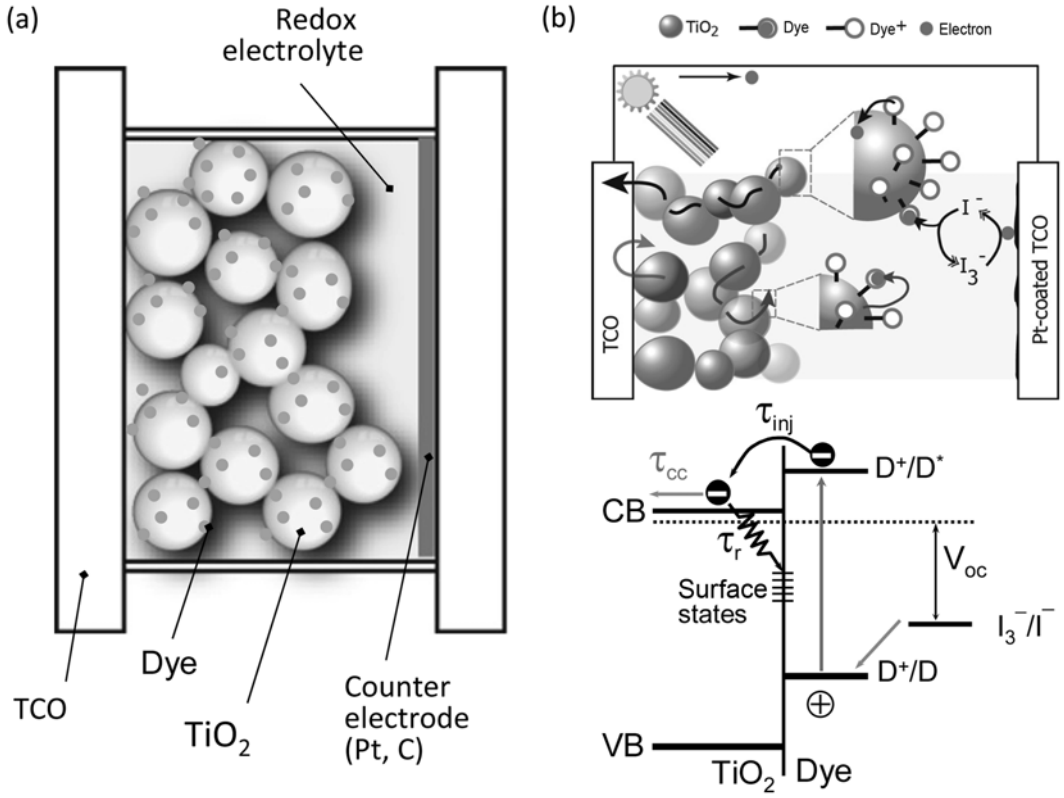

Fig. 1. (a) Structure and constituting materials and (b) working principle of dye-sensitized solar cell. In (b), the upper figure shows electron transport pathway and the lower figure represents energy position of each component in DSSC showing electron injection time constant (τ_{inj}), charge collection time constant (τ_{cc}) and time constant for recombination (τ_r).

is often referred to as quantum efficiency (QE), a collective measure of light harvesting efficiency, charge separation efficiency and charge collection efficiency. IPCE is defined as the ratio of the number of electrons collected by the solar cell to the number of photons of a given energy incident on the solar cell, which can be also expressed in terms of photocurrent density (J_{SC}), wavelwngth (λ) and input light intensity (P) as follows:

$$\mathrm{IPCE} = \frac{1240 \times J_{SC}(\mathrm{A/m^2})}{\lambda(\mathrm{nm}) \times \mathrm{P(W/m^2)}} \quad (1)$$

The relation in Eq. (1) is obtained by the following procedure. As mentioned previously, IPCE is defined as ratio of number of electrons to number of photons.

$$\mathrm{IPCE} = \frac{\text{Number of electrons (n)}}{\text{Number of photons (N)}} \quad (2)$$

In Eq. (2), multiplying q/s to estimate current per unit area gives Eq. (3), where q and s represent electron charge and unit area, respectively.

$$\mathrm{IPCE} = \frac{\mathrm{qn/s}}{\mathrm{qN/s}} = \frac{J_{SC}(\mathrm{A/m^2})}{\mathrm{qN/s/m^2}} \quad (3)$$

Incident power (P) in W/m^2 has the relation of $P(W/m^2)=N\times(hc/\lambda)$, which can be rearranged to be $N=(P\times\lambda)/hc$. IPCE is therefore expressed by Eq. (4).

$$\mathrm{IPCE} = \frac{J_{SC} \times hc}{q \times \lambda \times P} \quad (4)$$

Using the Planck constant (h) of 6.626×10^{-34} (Js), the speed of light (c) of 2.998×10^{8} (m/s) and the electron charge (q) of 1.602×10^{-19} (C=As), the number 1,240 in Eq. (1) can be obtained.

When taking the optical property into consideration, there are two QEs, that is, external quantum efficiency (EQE) and internal quantum efficiency (IQE). EQE includes the effect of optical losses by transmission and reflection, while IQE refers to the efficiency for the photons that are not reflected or transmitted out of the cell. From the reflection and transmission of a solar cell, EQE curve can be corrected to obtain the internal quantum efficiency curve. IPCE is related to EQE and therefore IPCE depends on the absorption of light as well as the collection of charges.

Conceptually similar to QE is the spectral response. The spectral response is defined as the ratio of the current generated by the solar cell to the power incident on the solar cell. Unlike the shape of QE curves, the spectral response decreases with decreasing wavelength because of increased photon energy. Spectral response is important since it is measured from a solar cell, and from this the quantum efficiency is calculated. The quantum efficiency can be determined from the spectral response (SR) by the relation in Eq. (5).

$$\mathrm{QE} = \frac{\mathrm{SR}}{\lambda} \times \frac{hc}{q} = \frac{\mathrm{SR}}{\lambda(\mathrm{nm})} \times 1240 \quad (5)$$

3. Light Harvesting Efficiency (LHE)

When the incident light (I_0) pass through the substance, it is in part absorbed by the substance and partly transmitted. Transmittance (T) of light is the ratio between the transmitted light intensity (I) and

the incident light intensity (I_0) and expressed by $T=I/I_0=\exp(-\alpha d)$, where α and d represent absorption coefficient and thickness of absorber. Light harvesting efficiency (LHE) is related to the absorption fraction $(I_0-I)/I_0$ and therefore can be expressed by Eq. (6).

$$LHE=1-e^{-\alpha d} \quad (6)$$

For instance, when dyes with extinction coefficient of 1.4×10^4 cm^2/mole at 530 nm are adsorbed on the 10 μm-thick TiO_2 film comprising 20 nm-diameter particles, LHE approaches over 99% [2].

NANOENGINEERING TECHNOLOGIES FOR IMPROVEMENT OF LIGHT HARVESTING EFFICIENCY

1. Light Scattering Method and Size-dependent Scattering Efficiency

In dye-sensitized solar cell, among the three important components, inorganic oxide film should be firstly considered. This is because photovoltaic performance depends significantly on kind of inorganic material, morphology of nanoparticle and inorganic oxide film porosity. Among the several candidates for photoanode materials, TiO_2 has been usually adapted as adequate material for DSSC since it has demonstrated best performance compared to other oxide materials. Nanocrystalline TiO_2 forms as anatase phase or rutile phase depending on synthetic procedure. Anatase nanocrystalline TiO_2 can be prepared hydrothermally under high pressure. Rutile nanocrystalline can be prepared by hydrolysis of $TiCl_4$ at ambient temperature [10]. Fig. 2 compares the morphologies of rutile and anatase TiO_2 films and their J-V characteristics [11]. As can be seen in Fig. 2(c), the short-circuit photocurrent density (J_{SC}) of the rutile-based solar cell (10.6 mA/cm^2) is about 30% less than that of the anatase-based cell (14 mA/cm^2) without difference in open-circuit voltage (V_{OC}). As a result, the overall energy conversion efficiencies are 5.6% and 7.1% for the rutile-based DSSC and anatase-based one, respectively. The J_{SC} difference is mainly due to the difference in morphology of particle, associated with surface area. In Figs. 2(a) and (b), the average dimension of the rod-shaped rutile particle (20×80 nm) is larger than that of the spherically shaped anatase particle with diameter of about 20 nm. In addition, the pore volume of the rutile films appears larger than that of the anatase film from the cross sectional SEM micrographs in Figs. 2(d) and (e). This implies that the surface area per unit volume of the rutile film is smaller than that of the anatase film. Therefore, the difference in J_{SC} between rutile-based DSSC and anatase-based one is due to difference in the amount of the adsorbed dye because of difference in particle morphology and film packing density. Nanoparticle packing structure is found to have influence on electron transport rate. The effective electron diffusion coefficient D_n is obtained from the relation $D_n=d^2/4\tau_{IMPS}$, where d and τ_{IMPS} are the film thickness and the time constant for electron transport measured by IMPS (intensity modulated photo-

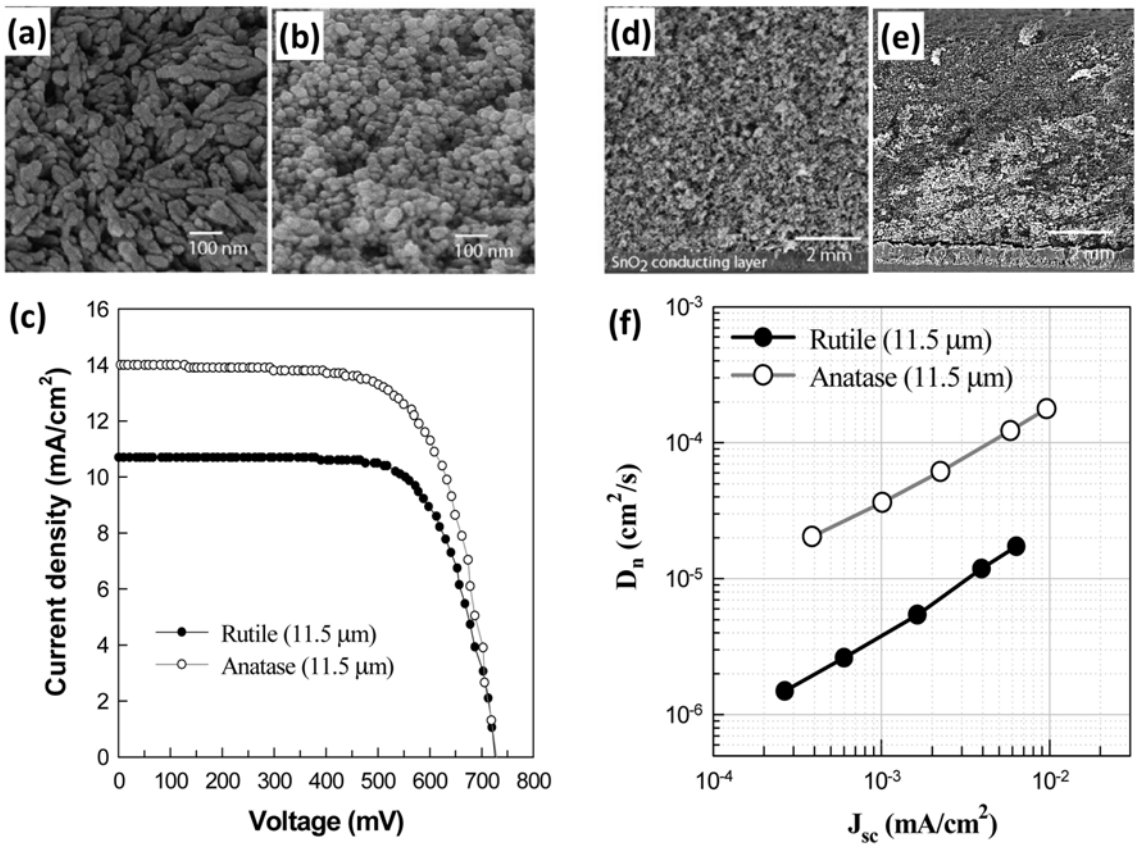

Fig. 2. Surface SEM micrographs for (a) rutile and (b) anatase TiO_2 film and (c) photocurrent-voltage property for the corresponding films sensitized with N719 dye. Cross section SEM micrographs for (d) rutile and (e) anatase TiO_2 film and (f) electron diffusion coefficients for the corresponding films sensitized with N719 dye.

current spectroscopy). In Fig. 2(f), it can be seen that at the same light intensity, represented by J_{SC}, the electron diffusion coefficient D_n for the rutile film is about one order of magnitude lower than that of the anatase film, which indicates that the photo-injected electrons move more slowly in the loosely packed rutile film than the compact structure of the anatase film. The difference in the rate of electron transport in these materials could be due to difference in the number of surface states or the extent of interparticle connectivity per unit film volume. It is reported that the transport of electrons through the nanostructured film is slowed by multiple trapping events, involving principally surface states [12-14], which indicates that increase in the surface state may retard the electron transport rate. If the number of surface states is the primary cause of the difference in the rate of electron transport in these materials, then one can expect that the surface area of the rutile film would be substantially larger than that of anatase. However, since the surface area of the rutile film is smaller than that of the anatase film, the absolute number of surface states can be ruled out as a cause for the difference in the rate of electron transport in rutile and anatase films. Therefore, the difference in electron transport rate between rutile and anatase films is due to the second possible factor relating to the relative number of interparticle connections. The rutile particles stack less efficiently than the anatase particles and that the rutile films have a lower number of interparticle connections per unit film volume than that of the anatase film. Thus, the number of pathways encountered by an individual electron is effectively smaller for a rutile film than for an anatase film. Restricting the number of conductive pathways through the particle network is expected to slow electron transport. This indicates that film porosity is important to control the electron transport rate in DSSC. The effect of porosity on electron transport behavior has been studied in detail [15].

Fig. 3 shows the effect of the anatase TiO_2 film thickness on photocurrent and transmittance. The studied films are prepared with autoclaved TiO_2 nanoparticles with average diameter of about 20 nm. As the film thickness increases from 6 μm to 12 μm, J_{SC} increases from 12 mA/cm^2 to 15 mA/cm^2, corresponding to 25% increment, and V_{OC} decreases from 0.87 V to 0.82 V, corresponding to about 6% decrease. For the case of lowered voltage is due to the increased surface states, acting as recombination centers [16-18], induced by the increased surface area. It is obvious that increase in film thickness improves photocurrent density. However, the increased photocurrent density is not doubled by increasing film thickness twice. When comparing transmittance of 6 μm- and 12 μm-thick films in Fig. 3(b), difference in transmittance decreases with increasing wavelength, that is to say, little difference at long wavelength ranging from 650 nm to 800 nm. For this reason, a TiO_2 film comprising only nanocrystalline particles cannot improve photocurrent density significantly by increasing simply the film thickness.

Instead of using only nanocrystalline TiO_2 particle films, it has been proposed that a bilayer structure composed of light scattering layer and nanocrystalline semitransparent layer can improve photocurrent density substantially due to the fact that the confinement of incident light by light scattering particles can gain more photons [19,20]. When light collides with the large TiO_2 particle having submicrometer size, the light scatters strongly (Mie scattering), which increases the path length of the incident light in the nanocrystalline TiO_2 films. Eventually, the scattering effect by introduction of the large TiO_2 particles is expected to enhance the photocurrent density and thereby overall conversion efficiency. The scattering effect is known to be dependent on size [21], refractive index [22] and position [23] of the scattering particles. Most studies on scattering efficiency in DSSCs [24-28] has also been investigated theoretically, in which it is proposed that the scattering is largest when the particle diameter is about $k\lambda$, where k is a constant and λ is the wavelength, that is, light scattering efficiency correlates with the size of the scattering particle in relation to the size of the wavelength of incoming light. We have first demonstrated the size-dependent scattering efficiency in dye-sensitized solar cell using a bilayer film structure with a scattering overlayer deposited on a semitransparent nanocrystalline TiO_2 main-layer [29]. Large scattering particles with rutile phase are compared, where SP1 and SP2 have particle size of about 0.3 μm and 0.5 μm, respectively. According to the photocurrent density-voltage (J-V) characteristics in terms of the size of the scattering rutile particles, the conversion efficiency is improved after deposition of the overlayer. The conversion efficiency of 7.55% for the 7 μm-thick TiO_2 film is improved to 8.94% and 8.78% after intro-

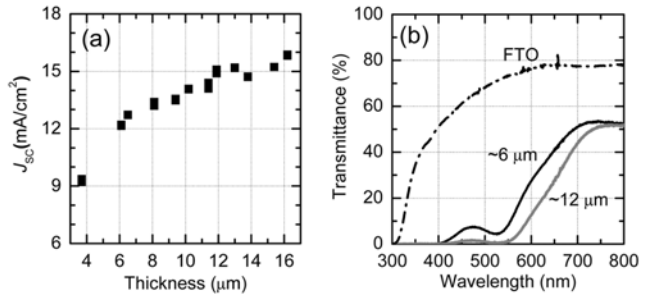

Fig. 3. (a) Dependence of photocurrent density on thickness of TiO_2 film comprising 20 nm-diameter TiO_2 nanoparticles and (b) transmittance of 6 μm-thick and 12 μm-thick TiO_2 films comprising 20 nm-diameter TiO_2 nanoparticles, along with that of FTO.

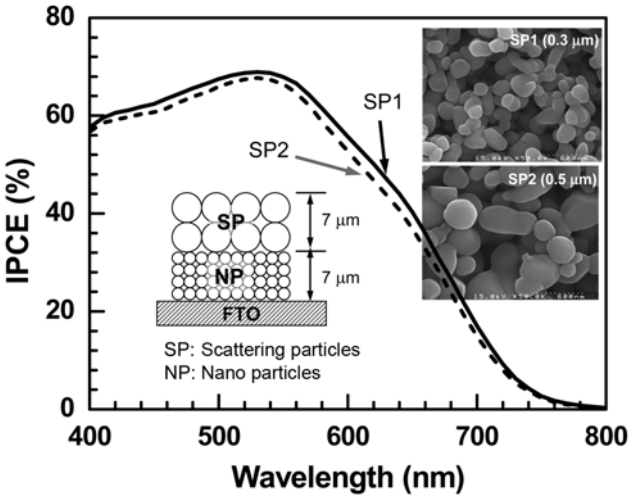

Fig. 4. IPCE spectra as a function of wavelength for 7 μm-thick nanocrystalline TiO_2 mainlayer-based films with 7 μm-thick overlayers consisting of SP1 and SP2 particles, where morphology and average particle size of SP1 and SP2 are shown in SEM micrographs.

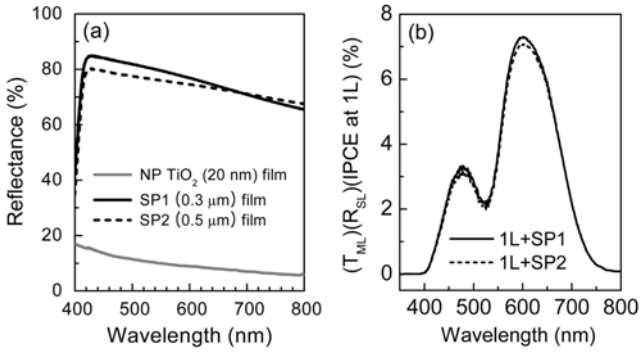

Fig. 5. (a) Reflectance spectra of the nanoparticulate TiO_2 (NP), SP1 and SP2 films and (b) calculated scattering efficiency for 7 μm-thick NP TiO_2 mainlayer (1L)-based SP1 and SP2 scattering layers.

duction of the scattering layers SP1 and SP2, respectively. Although SP1 is relatively smaller than SP2, SP1-conatined TiO_2 film shows a little bit higher efficiency. The improved efficiency is mainly caused by the increase in photocurrent density. Fig. 4 compares the IPCE spectrum of SP1-conatined film and SP2-contained one. SP1 particle overlayer shows better IPCE than SP2 one in the entire wavelength. The size-dependent scattering efficiency is therefore expected be related to the difference in reflectivity.

Fig. 5 shows the UV-VIS reflectance and the estimated scattering efficiency of the SP1 and SP2 particle films, along with a nanocrystalline TiO_2 film. Reflectance of the nanocrystalline TiO_2 film is negligible, while SP1 and SP2 scattering particles exhibit reflectance as high as 70-80% in the 400-800 nm. The reflectance of the SP1 particle film is higher than that of the SP2 particle in the 400-700 nm range. At the longer wavelength above 700 nm, SP2 particle shows higher reflectivity. When considering that the N719 dye used for DSSC utilizes photon energy with wavelength lower than 800 nm, SP1 is beneficial to light reflection in 300-800 nm wavelength range. We have calculated the scattering efficiency in order to clarify the dependence of particle size. Assuming the negligible charge generation by the scattering layer, the increased IPCE will be proportional to the transmitted light, reflected light and IPCE at the main layer. Accordingly, the scattering efficiency can be expressed simply by the following Eq. (7):

$$\text{Scattering efficiency}=(T_{ML})\times(R_{SL})\times(\text{IPCE at main-layer}) \quad (7)$$

where T_{ML} and R_{SL} represent transmittance of the main layer and reflectance of the scattering layer, respectively, and each value are taken from the UV-VIS and the reflectance data. The IPCE data without scattering layer are used for the IPCE at the main layer. In Fig. 5(b), the calculated scattering efficiency is compared, where scattering is enhanced at around 470 nm and 600-650 nm. The scattering efficiency for SP1-overlayered NP TiO_2 film is higher than that for SP2-overlayered one, which confirms again that the size-dependent scattering efficiency is apparent. From the estimated scattering efficiency in Fig. 5(b), it can be found that scattering particle size is related to half of wavelength at maximum scattering efficiency.

2. Bi-functional Materials Having Light Scattering and Charge Generation Properties

As we investigated previously, large TiO_2 particles with spherical shapes or flat surfaces are normally used as the scattering particles. Although large-sized particle plays an important role in light scattering, such a low-surface-area scattering particle hardly offer any additional effect, for instance electron generation, because dye adsorption is expected to be much less for these particles than for nanocrystalline TiO_2. To exhibit both light-scattering and electricity-generation properties, nano-embossed hollow spherical TiO_2 (NeHS TiO_2) is developed for use as bi-functional material in DSSC [4]. NeHS TiO_2 can be synthesized in a 0.2 M tetrabutyl ammonium hydroxide (TBAH) environment during a solvothermal reaction without addition of any templates or surfactants. Fig. 6 shows SEM and TEM images of the as-synthesized NeHS TiO_2 particles. The diameter of the spheres is in the range of 1-3 μm. TEM image obtained by using a microtome technique shows that each NeHS TiO_2 particle has a hollow-sphere structure with a wall thickness of ca. 250 nm. The hollow spheres consist of TiO_2 nanoparticles with an average diameter of about 18 nm. The synthesized NeHS TiO_2 phase

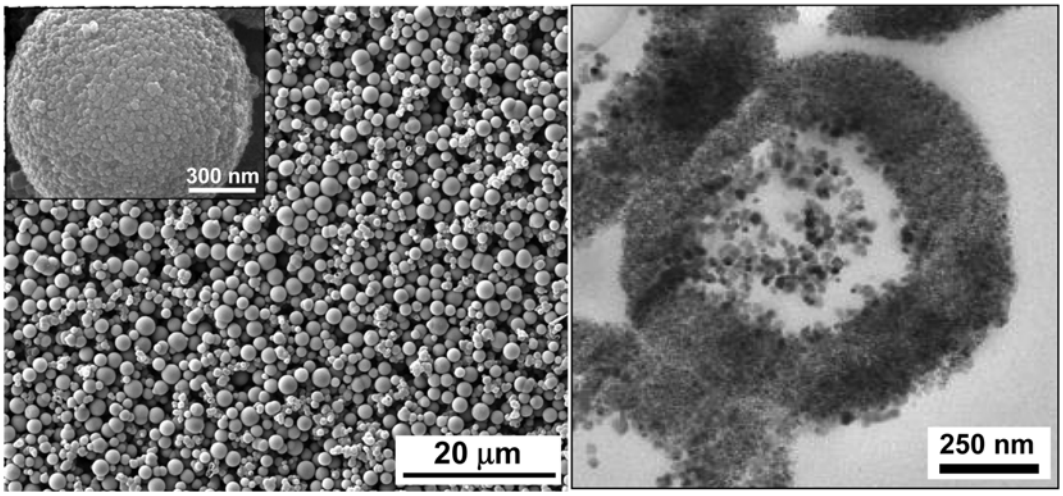

Fig. 6. SEM micrographs showing (left) size distribution, surface morphology (inset) and (right) inside structure of nano-embosed Hallow sphere (NeHS) TiO_2 particles.

exists in the anatase form confirmed by X-ray diffraction (XRD) analysis. BET measurement shows that the average pore size is about 10 nm and the surface area is determined to be 58 m^2/g.

Bi-layer structure is used to investigate the effect of the NeHS TiO_2 morphology on the photovoltaic properties. The photovoltaic property of the nanocrystalline TiO_2 underlayer/NeHS TiO_2 overlayer (1L-NeHS) is compared with that of the the nanocrystalline TiO_2 underlayer/flat-surface-400 nm-sized TiO_2 overlayer (1L-CCIC). The total film thicknesses are adjusted to be about 12 μm. As can be seen in Fig. 7(a), IPCE for the 1L-NeHS shows higher than that for the 1L-CCIC in the entire wavelength. The photovoltaic performance of 1L-NeHS shows a higher J_{SC} than 1L-CCIC but similar V_{OC} to 1L-CCIC. As a result, the conversion efficiency of 1L-NeHS is better than both that for 1L-CCIC. The higher J_{SC} is probably related to either the amount of adsorbed dye or light scattering or both. The amount of adsorbed dye for the 1L-NeHS film is estimated to be about 1.266×10^{-7} mol/cm^2, which is 57% higher than that for the 1L-CCIC film (0.805×10^{-7} mol/cm^2). Therefore, the higher J_{SC} observed for 1L-NeHS than 1L-CCIC is partly attributed to the larger quantity of dye on the NeHS particles.

Fig. 7(b) compares the UV-VIS reflectance spectrum of the dye-adsorbed NeHS TiO_2 films with those of the dye-adsorbed CCIC TiO_2 and the dye-adsorbed nanocrystalline TiO_2 films, where the film thicknesses are the same. The reflectance of the NeHS TiO_2 film decreases drastically and resembles that of the dye-adsorbed nanocrystalline TiO_2 film in the short wavelength ranging from 400 to 600 nm, which is mainly due to light absorption by the dye molecules. On the other hand, the CCIC TiO_2 film shows a high reflectance at 400-600 nm because of low dye adsorption. In the long wavelength region, the dye-adsorbed NeHS film exhibits a substantially higher reflectance than the dye adsorbed nanocrystalline TiO_2 film and its reflectivity is close to that of the CCIC film. The reflectance spectroscopic study indicates that NeHS particle has bi-functionality of light scattering and charge generation.

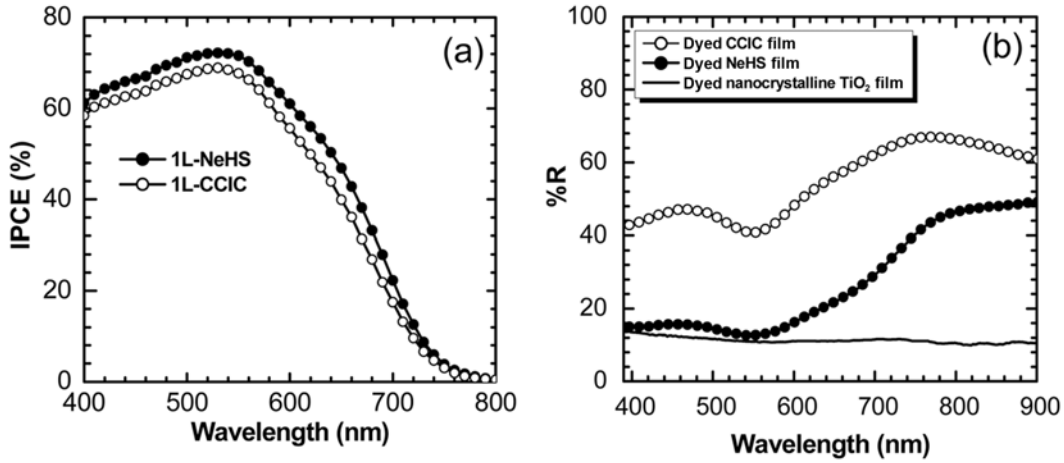

Fig. 7. (a) IPCE spectra of DSSCs based on the nanoparticulate TiO_2 mainlayer (1L)-based bilayer structure having an overlayer of nano-embossed hollow sphere TiO_2 particles (1L-NeHS) and flat-surface submicrometer-sized TiO_2 particles (1L-CCIC). (b) Diffused reflectance spectra of NP, CCIC, and NeHS TiO_2 particulate films covered with N-719 dye.

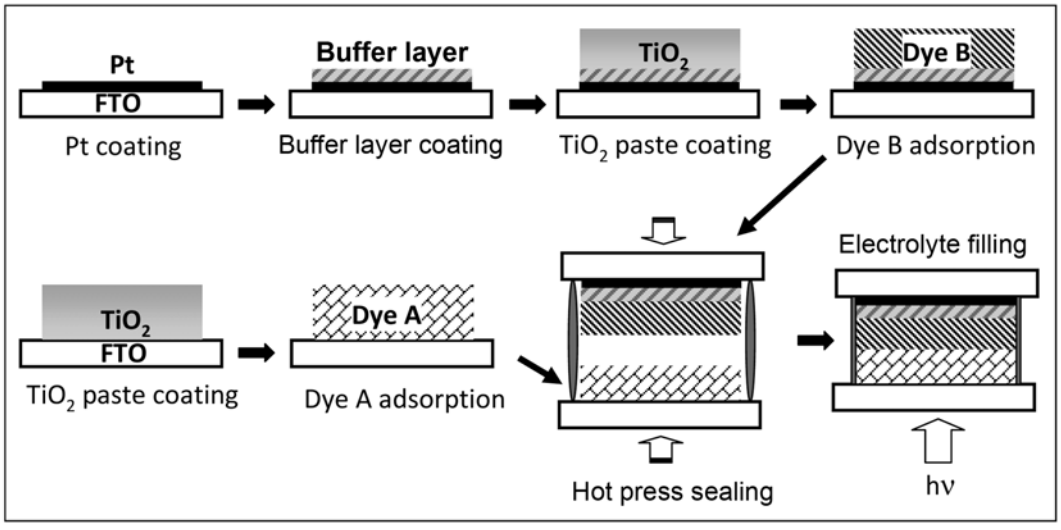

Fig. 8. Procedure of heterosensitizer junction DSSC, where dye A is adsorbed on the working electrode side and dye B is on the counter electrode side. A-dyed layer and B-dyed layer are physically contacted using hot pressure.

3. Heterosensitizer Junction

Two different dyes with complementary absorption characteristics are expected to better in light harvesting than single dye because absorption range will be extended. The well-known DSSC fabrication procedure allows only single dye adsorption since high-temperature annealing process is involved for making TiO_2 film. If we adopt such a conventional procedure for fabricating DSSC with two different dyes, the first dye adsorbed on the first TiO_2 layer will be decomposed because of high temperature annealing process for the second TiO_2 layer for the second dye adsorption. Therefore, it may be hard to introduce two different dyes in a mesoporous TiO_2 film from the conventional fabrication procedure. For this reason, instead of sequential arrangement of dyes, most reported structures were based on dye-cocktail (co-sensitization) method [30-34]. Recently, a new technology has been developed to organize two different dyes sequentially [35].

Fig. 8 shows the fabrication procedure of a heterosensitizer junction DSSC. A heterosensitizer junction structure can be prepared as follows: two TiO_2 layers are separately formed on a FTO substrate and a Pt-coated FTO substrate. One TiO_2 layer, designated as A layer, forms on a FTO substrate, and the other TiO_2 layer, designated as B layer, forms on the Pt-coated FTO substrate. The A layer is sensitized with a TA-St-CA dye having a relatively large HOMO-LUMO gap energy [36], this is, short wavelength sensitizer with maximum absorption at 400 nm. The B layer is covered with a relatively longer wavelength sensitizer a N-719 dye having maximum absorption at 530 nm. These two different dye-sensitized electrodes are assembled using surlyn (Dupont 1702) at a pressure of 200 kPa/cm^2 and a temperature of about 120 °C within a few seconds. An electrolyte solution composed of 0.7 M 1-butyl-3-methyl-imidazolium iodide, 0.03 M I_2, 0.1 M guanidinium thiocyanate, and 0.5 M 4-tert-butylpyridine in acetonitrile and valeronitrile 85 : 15 v/v is introduced. The TiO_2 film thickness is adjusted to 5 μm and 4 μm for the dye A layer and the dye B layer, respectively, and 9 μm-thick TiO_2 film is used for the single dye (dye A) structure.

The I-V measurement confirms that the heterosensitizer junction structure exhibits J_{SC} of 9.7 mA/cm^2, V_{OC} of 0.741 V, fill factor of 0.538 and efficiency (η) of 3.86%, whereas the single dye A-contained solar cell shows 7.7 mA/cm^2, 0.755 V, 0.635 and 3.7%. Photocurrent-density of the heterosensitizer-junction structure is 26% higher than that of the single dyed solar cell, which is likely to be due to wide-band absorption by dye A (TA-St-CA) and dye B (N-719). The contribution from dye A and dye B to photocurrent generation is clearly seen in the IPCE spectrum, as can be seen in Fig. 9(a), where, compared to the IPCE spectrum of the single dye A-contained DSSC, the heterosensitizer junction shows higher IPCE at the wavelength above 500 nm. The IPCE values are similar at 450 nm, whereas IPCE value of the two dyed structure at 600 nm (18.1%) is substantially higher than that of the single dyed one (1.1%).The IPCE observed at the wavelength longer than 600 nm is thus resulted from injection of the photo-excited electrons in N-719 dye since only N-719 absorbs longer wavelength lights as shown in Fig. 9(b).

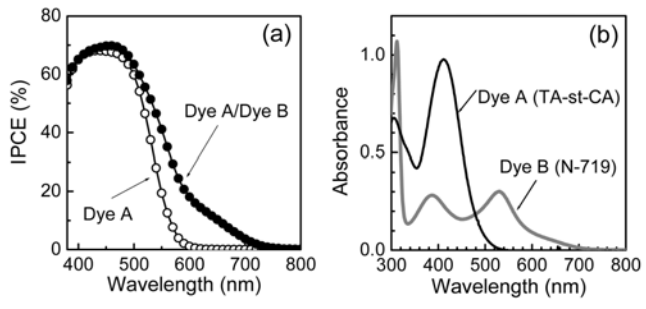

Fig. 9. (a) IPCEs of heterosensitizer junction DSSC (dye A/dye B) and single dyed (dye A) DSSC and (b) UV-Vis spectra of dye A and dye B.

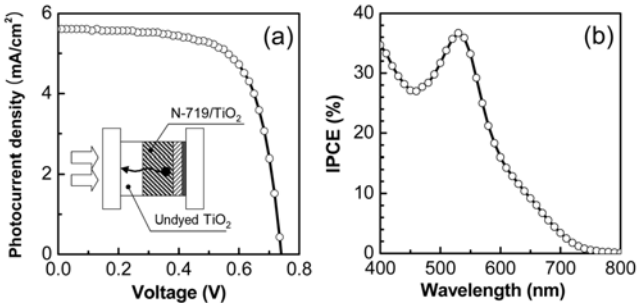

Fig. 10. (a) Photocurrent density-voltage curve and (b) IPCE of the heterosensitizer junction-type DSSC with dye B adsorbed TiO_2 film on the counter electrode side and bare TiO_2 film (undyed) on the working electrode side.

In order to confirm whether the electrons generated in the B layer are transported through the A layer, a cell structure having a bare A layer (3 μm-thick TiO_2 layer without dye A) and a N-719 adsorbed 6 μm-thick B layer is designed. Fig. 10 shows the J-V curve and IPCE spectrum, where the schematic cell structure is shown in the inset of Fig. 10(a). Photocurrent-voltage curve and IPCE confirm that the electrons generated in the B layer are apparently collected to the FTO substrate through the undyed TiO_2 (bare A) layer. Effect of A-layer thickness is also investigated, where the photocurrent is found to be slightly decreased with increasing the undyed A layer thickness. From the IPCE study, such a gradual decrease in photocurrent density is associated with less utilization of short wavelength light due to the increased A-layer thickness. It is evident from the study with specially designed cells that the photo-excited electrons in the B layer are obviously transported to the working electrode.

4. Selective Positioning of Three Different Dyes

In the case of DSSC, sequential adsorption of several dyes, taking account of the absorption properties of each dye, in a single TiO_2 mesoporous electrode is an ideal design to extend the range of light absorption, called panchromatic absorption. Previously, we show a method to have two different dyes in a dye-sensitized solar cell structure as one of panchromatic approaches. This method, however, does not seem to allow more than two dyes. Therefore, a new methodology is required to arrange multi dyes sequentially in a TiO_2 layer. Here, we introduce a new method for selective positioning of organic dye molecules with different absorption ranges in a mesoporous TiO_2 film [37]. The key technology in this method is how to desorb selectively the adsorbed dye, which starts from a simple idea mimicking column chromatography. Control of retention time during separation of substances in mobile phase may be dependent on the por-

osity of the stationary phase in column chromatograph. The polystyrene-filled mesoporous TiO_2 film is explored for use as a stationary phase and a Bronstead base-contained polymer solution is developed for use as a mobile phase for selective desorption of the adsorbed dye. Dye solution and NaOH aqueous solution mixed with polypropylene glycol (PPG) are used as mobile phases for selective adsorption and desorption, respectively. Three dyes are tried to be positioned in a TiO_2 layer: 2-cyano-3-(5-(4-ethoxyphenyl)thiophen-2-yl)acrylic acid (referred to as P5, yellow colour) with the absorbance property of short wavelength light, cis-bis (isothiocyanato) bis (2,2′-bipyridyl-4,4′-dicarboxylic acid) ruthenium(II) (referred to as N719, red colour) with the absorbance property of middle wavelength light, and tri(isothiocyanato)(2,2′;6′,2″-terpyridyl-4,4′,4″-tricarboxylic acid) ruthenium(II) (referred to as N749, green colour) with the absorbance property of long wavelength light. Firstly two dyes of N719 and N749 are used to find out how to control the depth of the dye-desorbed layer. The detailed procedure is as follows. N719 dye is first adsorbed on an annealed TiO_2 film, and then polystyrene is formed inside the TiO_2 film to decrease the pore size by means of polymerization of styrene oligomer adsorbed on TiO_2 surface. The reduced pore size in TiO_2 film, confirmed by Scanning electron microscope (SEM) and electron probe micro analyzer (EPMA), allows us to control the desorption and second adsorption depths of the dye molecules. For selective desorption to remove N719 from the upper region of the TiO_2 film, the solution is prepared by mixing NaOH aqueous solution and poly(propylene glycol) (PPG). The use of PPG is to slow down the penetration rate of NaOH aqueous solution and thereby the thickness of desorbed layer is controlled. N749 dye is adsorbed on the N719-desorbed region. After completion of the selective adsorption, polystyrene is removed by solvating the coiled polymer chain using ethyl acetate solution.

Based on the developed method, the selective positioning of three dyes with different absorbance characteristics, P5 (yellow), N719 (red), and N749 (green) is performed. Since the longer wavelength light can reach the TiO_2 layer far away from the FTO substrate, the dye alignment is designed to be the following order: FTO/P5/N719/N749. In Fig. 11(a), EPMA measurements confirm the formation of P5 dye on the bottom of the TiO_2 film, N719 in the middle and N749 on the top. J-V curves in Fig. 11(b) shows that the three dyed cell exhibits highest photocurrent density compared to each single dye cell. Fig. 11(c) displays IPCE spectra for the P5 dye positioned on the bottom of the TiO_2 film with a thickness of about 9 μm, the N719 dye aligned in the middle of the film with a thickness of about 9 μm, the N749 dye that is positioned on the top of the film with a thickness of about 7 μm and the selectively positioned three dyes. The IPCE spectral shape of the resulting three dyed cell shows well superimposition of each IPCE spectrum from a single dyed cell.

It is interesting to see the difference in open-circuit voltage of each single dyed cell and three dyed cell from the J-V curves in Fig. 11(b). When considering that V_{OC} is determined by the difference between the Fermi energy level of TiO_2 and the redox potential of electrolyte, one can expect that there is little difference in V_{OC} since we use the same TiO_2 and electrolyte for each single dyed cell and three dyed cell. Contrary to the expectation, all the measured volt-

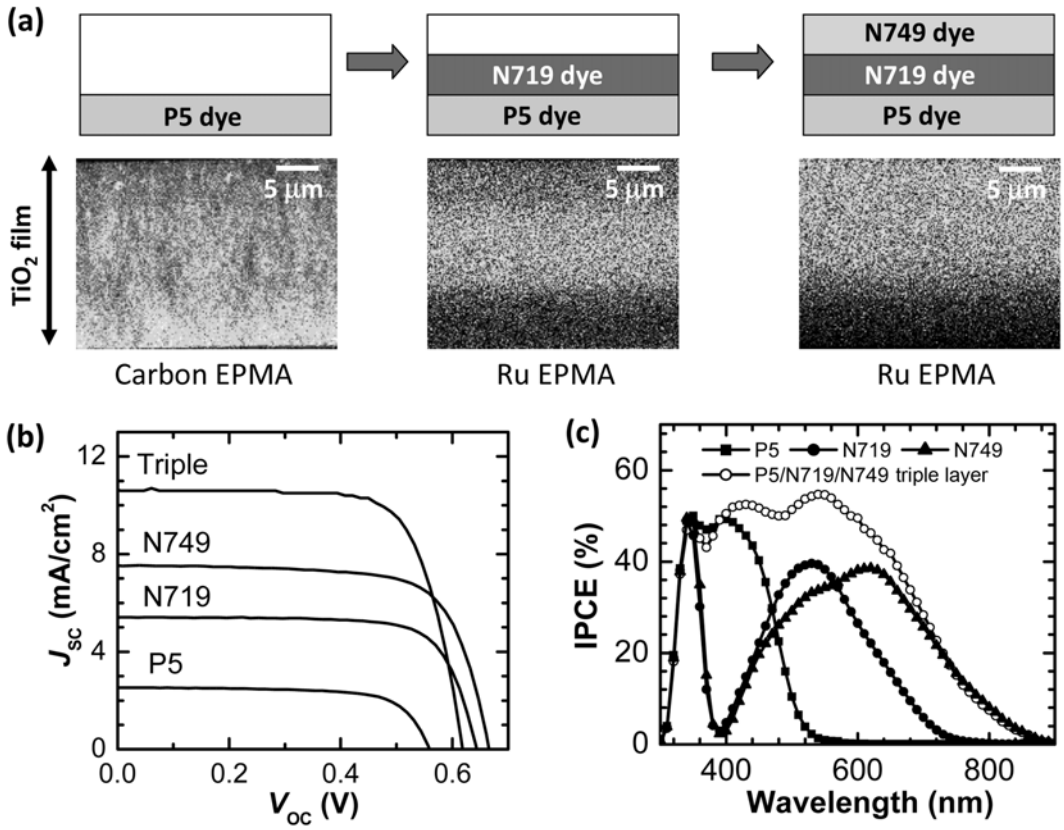

Fig. 11. (a) Carbon and Ruthenium EPMA spectra showing adsorption and desorption of dyes. (b) Photocurrent density-voltage curves and (c) IPCE spectra for each single dyed DSSC (P5, N719 and N749) and three dyed DSSC (Triple layer).

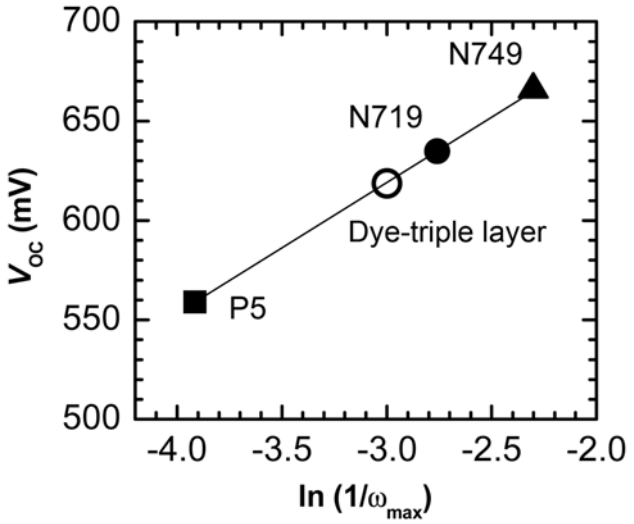

Fig. 12. Dependence of V_{OC} on logarithm of reciprocal maximum frequency (ω_{max}) for each single dyed DSSC (P5, N719 and N749) and three dyed DSSC (triple layer). ω_{max} is obtained from the electrical impedance spectra.

ages are different. This underlines that the Fermi energy level of TiO_2 is varied with dye when assuming the the redox potential is not changed. Since Fermi energy level can be influenced by TiO_2-electrolyte interfacial charge transfer kinetics, electrochemical impedance spectroscopy study could address this issue. In DSSC, the second semicircle of the Nyquist plots is usually known to be attributed to the back reaction of injected electron transfer at the TiO_2/dye/electrolyte interface [8,38,39]. It is generally accepted that an increase (or decrease) in the frequency at the maximum imaginary resistance of the second semicircle (ω_{max}) correlates with decreased (or increased) V_{OC}, which is due to the accelerated (or retarded) back reaction at open-circuit conditions under illumination. The V_{OC} of a DSSC can be expressed as Eq. (8) [40]:

$$V_{OC} = \frac{RT}{\beta F} \ln\left(\frac{AI}{n_0 k_b [I_3^-] + n_0 k_r [D^+]}\right) \quad (8)$$

where R is the molar gas constant, T is the temperature, F is the Faraday constant, β is the reaction order for I_3^- and electrons, A is the electrode area, I is the incident photon flux, n_0 is the concentration of accessible electronic states in the conduction band, and k_b and k_r are the kinetic constant of the back reaction of the injected electrons with triiodide and the recombination of these electrons with oxidized dyes (D^+), respectively. Considering that the ω_{max} is same as the back reaction constant (k_b) [41], the V_{OC} will depend logarithmically on the $1/\omega_{max}$ as the loss term ($n_0 k_r [D^+]$) can be neglected. Fig. 12 shows the observed V_{OC} as a function of $\ln(1/\omega_{max})$. The observed V_{OC} is proportional to $\ln(1/\omega_{max})$, which suggests that the open-circuit voltage of the solar cell with selectively aligned three different dyes is related to the interfacial charge transfer rate.

SUMMARY

Technologies for improvement of light harvesting efficiency are described. Light scattering method is found to a useful way to utilize long wavelength light. Bi-layer structure comprising the nano-sized particulate film as a bottom layer and the sub-micron-sized particulate film as a top layer enhances light scattering efficiency, where particle size in the top layer is found to have an influence on scattering efficiency. Nano-embossed hallow sphere is one of good candidates for dual functions of both light scattering and charge generation. To cover wide range of incoming light, method of selective positioning of dyes with different absorption characteristics is developed. Selective desorption is realized by controlling retention time of dye adsorption and desorption solutions by means of downsizing pore of TiO_2 film and exploring viscous NaOH solution. Panchromatic absorption is realized by this selective positioning of organic sensitizers in a mesoporous inorganic film. By combining this panchromatic absorption technology with light scattering method and bi-functional nano-engineering approach, dye-sensitized solar cell with overall conversion efficiency higher than current 11% is expected.

REFERENCES

1. B. O'Regan and M. Gratzel, *Nature*, **353**, 737 (1991).
2. M. Gratzel, *Inorg. Chem*., **44**, 6841 (2005).
3. Y. Chiba, A. Islam, Y. Watanabe, R. Komiya, N. Koide and L. Han, *Jpn. J. Appl. Phys. Part 2*, **45**, L638 (2006).
4. H.-J. Koo, Y. J. Kim, Y. H. Lee, W. I. Lee, K. Kim and N.-G. Park, *Adv. Mater*., **20**, 195 (2008).
5. N.-G. Park and K. Kim, *Phys. Stat. Sol. (a)*, **205**, 1895 (2008).
6. M. J. de Wild-Scholten and A. C. Veltkamp, ECN report (2007).
7. PV FAQs in US DOE (www.nrel.gov/docs/fy05osti/37322.pdf).
8. J. van de Lagemaat, N.-G. Park and A. J. Frank, *J. Phys. Chem. B*, **104**, 2044 (2000).
9. D. Cahen, G. Hodes, M. Gratzel, J. F. Guillemoles and I. Riess, *J. Phys. Chem. B*, **104**, 2053 (2000).
10. N.-G. Park, G. Schlichthorl, J. van de Lagemaat, H. M. Cheong, A. Mascarenhas and A. J. Frank, *J. Phys. Chem. B*, **103**, 3308 (1999).
11. N.-G. Park, J. van de Lagemaat and A. J. Frank, *J. Phys. Chem. B*, **104**, 8989 (2000).
12. P. E. de Jongh and D. Vanmaekelbergh, *J. Phys. Chem. B*, **101**, 2716 (1997).
13. N. Kopidakis, E. A. Schiff, N.-G. Park, J. van de Lagemaat and A. J. Frank, *J. Phys. Chem. B*, **104**, 3930 (2000).
14. Nelson, *J. Phys. Rev. B*, **59**, 15374 (1999).
15. K. D. Benkstein, N. Kopidakis, J. van de Lagemaat and A. J. Frank, *J. Phys. Chem. B*, **107**, 7759 (2003).
16. S. Y. Huang, G. Schlichthorl, A. J. Nozik, M. Gratzel and A. J. Frank, *J. Phys. Chem. B*, **101**, 2576 (1997).
17. S. Ito, T. Kitamura, Y. Wada and S. Yanagida, *Sol. Energy Mater. Sol. Cells*, **76**, 3 (2003).
18. J. Nissfolk, K. Fredin, A. Hagfeldt and G. Boschloo, *J. Phys. Chem. B*, **110**, 17715 (2006).
19. S. Ito, S. M. Zakeerudiin, R. Humphry-Baker, P. Liska, P. Charvet, P. Comte, M. K. Nazeeruddin, P. Pechy, M. Takata, H. Miura, S. Uchida and M. Gratzel, *Adv. Mater*., **18**, 1202 (2006).
20. S. Hore, C. Vetter, R. Kern, H. Smit and A. Hinsch, *Sol. Energy Mater. Sol. Cells*, **90**, 1176 (2006).
21. W. E. Vargas, *J. Appl. Phys*., **88**, 4079 (2000).
22. S. Hore, C. Vetter, R. Kern, H. Smit and A. Hinsch, *Sol. Energy Mater. Sol. Cells*, **90**, 1176 (2006).

23. Z.-S. Wang, H. Kawauchi, T. Kashima and H. Arakawa, *Coord. Chem. Rev.*, **248**, 1381 (2004).
24. A. Usami, *Chem. Phys. Lett*., **277**, 105 (1997).
25. A. Usami, *Sol. Energy Mater. Sol. Cells*, **64**, 73 (2000).
26. J. Ferber and J. Luther, *Sol. Energy Mater. Sol. Cells*, **54**, 265 (1998).
27. A. Usami, *Sol. Energy Mater. Sol. Cells*, **59**, 163 (1999).
28. W. E. Vargas and G. A. Niklasson, *Sol. Energy Mater. Sol. Cells*, **69**, 147 (2001).
29. H.-J. Koo, J. Park, B. Yoo, K. Yoo, K. Kim and N.-G. Park, *Inorg. Chim. Acta*, **361**, 677 (2008).
30. C. Tedeschi, F. Caruso, H. Möhwald and S. Kirstein, *J. Am. Chem. Soc*., **122**, 5841, (2000).
31. K. Sayama, S. Tsukagoshi and T. Mori, *Sol. Energy Mater. Sol. Cells*, **80**, 47 (2003).
32. J.-H. Yum, S.-R. Jang, P. Walter, T. Geiger, F. Nueesch, S. Kim, J. Ko, M. Graetzel and M. K. Nazeeruddin, *Chem. Comm*., 4680 (2007).
33. D. Kuang, P. Walter, F. Nueesch, S. Kim, J. Ko, P. Comte, S. M. Zakeeruddin, M. K. Nazeeruddin and M. Graetzel, *Langmuir*, **23**, 10906 (2007).
34. B.-Q. Liu, X.-P. Zhao and W. Luo, *Dyes and Pigments*, **76**, 327 (2008).
35. H.-J. Koo, K. Kim, N.-G. Park, S. Hwang, C. Park and C. Kim, *Appl. Phys. Lett*., **92**, 142103 (2008).
36. S. Hwang, J. H. Lee, C. Park, H. Lee, C. Kim, C. Park, M.-H. Lee, W. I. Lee, J. Park, K. Kim, N.-G. Park and C. Kim, *Chem. Comm*., 4887 (2007).
37. K. Lee, S. W. Park, M. J. Ko, K. Kim and N.-G. Park, *Nature Mater.*, **8**, 665 (2009).
38. R. Kern, R. Sastrawan, J. Ferber, R. Stangl and J. Luther, *Electrochim. Acta*, **47**, 4213 (2002).
39. F. Fabregat-Santiago, J. Bisquert, G. Garcia-Belmonte, G. Boschloo and A. Hagfeldt, *Sol. Energy Mater. Sol. Cells*, **87**, 117 (2005).
40. Q. Wang, J.-E. Moser and M. Gratzel, *J. Phys. Chem. B*, **109**, 14945 (2005).
41. M. Adachi, M. Sakamoto, J. Jiu, Y. Ogata and S. Isoda, *J. Phys. Chem. B*, **110**, 13872 (2006).